Water Research 307 (2026) 126731

Contents lists available at ScienceDirect

Water Research

journal homepage: www.elsevier.com/locate/watres

Post-regeneration neutralization enables stable phosphate adsorption-desorption in Ca- and NOM-rich waters

Yuwei Huang [a,b,c,*], Carlo Belloni [a], Leon Korving [a], A. Iulian Dugulan [c], Niels H. van Dijk [c], Doris van Halem [b]

[a] Wetsus, European Centre of Excellence for Sustainable Water Technology, Oostergoweg 9, Leeuwarden, 8911 MA, the Netherlands
[b] Water Management Department, Faculty of Civil Engineering and Geosciences, Delft University of Technology, Stevinweg 1, Delft, 2628 CN, the Netherlands
[c] Fundamental Aspects of Materials and Energy, Faculty of Applied Sciences, Delft University of Technology, Mekelweg 15, Delft, 2629 JB, the Netherlands

HIGHLIGHTS

- Post-regeneration neutralization mechanisms were examined in P-removal cycles.
- Residual alkalinity drives Ca-based precipitation and adsorbent deterioration.
- Acid-assisted neutralization stabilizes multi-cycle P removal in Ca/NOM-rich waters.
- Ca enhances reversible P removal when residual alkalinity is reduced.
- Neutralization prevents deterioration rather than removing aged precipitates.

GRAPHICAL ABSTRACT

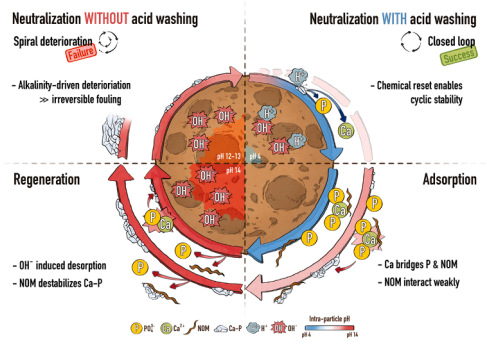

ARTICLE INFO

Keywords:
Phosphorus recovery
Wastewater treatment
Adsorbent regeneration
Calcium precipitation
Pore blockage
Residual alkalinity control

ABSTRACT

Residual alkalinity left after alkaline regeneration is a critical yet often overlooked factor controlling the long-term performance of iron-oxide adsorbents for phosphorus (P) removal and recovery. In porous adsorbents, incomplete neutralization can maintain a local alkaline environment, promoting calcium (Ca)-based precipitation and performance deterioration. This study evaluated post-regeneration neutralization of the iron oxide adsorbent GEH in Ca- and natural organic matter (NOM)-containing water matrices. Three neutralization conditions were compared: rapid rinsing, thorough washing, and acid-assisted neutralization. Rapid rinsing and thorough washing left residual alkalinity within GEH, driving Ca-based precipitation and progressive loss of adsorption capacity and regeneration efficiency. In contrast, acid-assisted neutralization largely reduced residual alkalinity, suppressed precipitation, and maintained adsorption-dominated P removal. Under acid-assisted neutralization, GEH sustained stable P removal of 4.51–5.83 mg/g with 88%–96% regeneration efficiency over 12 cycles in Ca- and NOM-containing systems. These findings identify post-regeneration neutralization as a preventive control step for residual alkalinity, rather than a delayed corrective treatment for accumulated precipitates, providing a practical strategy to improve the stability of adsorption-based P removal and recovery.

* Corresponding author.
E-mail address: Y.Huang-10@tudelft.nl (Y. Huang).

https://doi.org/10.1016/j.watres.2026.126731
Received 29 May 2026; Received in revised form 11 August 2026; Accepted 14 August 2026
Available online 15 August 2026

1. Introduction

Phosphorus (P) management is a critical concern in wastewater treatment. While P is essential for agriculture, excessive discharge causes eutrophication, harmful algal blooms, and water quality deterioration (Schindler, 1977). Among available removal technologies, adsorption using iron-based materials has gained attention due to its high efficiency at low concentrations, operational simplicity, and potential for P recovery (Belloni et al., 2023; Suresh Kumar et al., 2019b). Regenerable iron oxide adsorption processes are increasingly considered for tertiary P polishing and recovery from municipal wastewater (Suresh Kumar et al., 2018, 2019b; Wang et al., 2024). As these technologies progress toward pilot- and demonstration-scale implementation, efficient regeneration and reuse over multiple cycles become critical operational challenges (Oosterhuis et al., 2026). Current research has predominantly focused on enhancing phosphate (PO_4^{3-}) adsorption (Cui et al., 2023; Li et al., 2018), while the role of regeneration and post-regeneration neutralization in long-term performance remains insufficiently understood (Kunaschk et al., 2015; Suresh Kumar et al., 2018).

Alkaline regeneration using NaOH is widely employed to desorb P and recover adsorbent activity (Wang et al., 2024), but it can leave residual alkalinity within the porous structure of the adsorbent. Post-regeneration neutralization is applied to remove residual regenerant, but hydroxide (OH^-) can remain even after extensive rinsing (Ai et al., 2023; Suresh Kumar et al., 2018), altering surface charge and promoting pore-blocking precipitates (Antelo et al., 2015; Gao et al., 2023; Kunaschk et al., 2015). Previous studies have mainly used acid treatments as corrective steps to dissolve accumulated Ca-containing precipitates and recover P blocked by these precipitates (Kunaschk et al., 2015; Suresh Kumar et al., 2018). The role of acid-assisted neutralization after alkaline regeneration as a preventive residual-alkalinity control step has received less attention. This study therefore examines post-regeneration neutralization not as delayed deposit removal, but as a preventive operational control of residual alkalinity, Ca-P precipitation, pore blockage, and long-term cyclic performance.

In addition to regeneration effects, wastewater composition, particularly calcium (Ca) and natural organic matter (NOM), further complicates adsorbent performance (Cui et al., 2023; Suresh Kumar et al., 2018). Ca plays a dual role: it can enhance P adsorption by increasing positive surface charge or acting as a bridging cation (Antelo et al., 2015; Lin et al., 2017a), but it can also promote Ca-P precipitation under alkaline conditions, reducing adsorption reversibility (Antelo et al., 2015; Cui et al., 2023; Kunaschk et al., 2015). NOM may affect P removal through site competition, surface coverage, interactions with Ca, and modification of Ca-P deposition (Lei et al., 2018; Lin et al., 2005; Sindelar et al., 2015). However, previous studies have reported inconsistent NOM effects, ranging from limited influence to significant inhibition of phosphate adsorption, depending on NOM properties and water chemistry (Deng et al., 2019; Song et al., 2006). Therefore, the combined effects of Ca and NOM, especially during long-term adsorption-regeneration under residual-alkalinity conditions, remain unclear.

This study addresses these gaps by treating post-regeneration neutralization as a preventive residual-alkalinity control step rather than a corrective precipitate-removal treatment. Rapid water rinsing, thorough water washing, and acid-assisted neutralization were used to create different levels of residual alkalinity within GEH after NaOH regeneration. By comparing these conditions in Ca- and NOM-containing waters, we aimed to determine how residual alkalinity governs the balance between reversible phosphate adsorption and Ca-P precipitation during repeated adsorption-regeneration cycles. These findings provide mechanistic insight and practical guidance for designing regeneration protocols that prevent performance deterioration and maintain stable P removal and recovery.

2. Materials and methods

2.1. Chemicals and adsorbents

Potassium dihydrogen phosphate (KH_2PO_4), dipotassium hydrogen phosphate (K_2HPO_4), calcium chloride dihydrate ($CaCl_2{\cdot}2H_2O$), 1 M hydrochloric acid (HCl), and 1 M sodium hydroxide (NaOH) were obtained from VWR Chemicals. Suwannee River NOM (2R101N) was obtained as a dry solid extract from the International Humic Substances Society, and its concentration was expressed in terms of dissolved organic carbon (DOC). The P, Ca, and NOM (filtered through a 0.45 μm membrane) stock solutions were prepared using demineralized water at 140 mg/L, 600 mg/L, and 600 mg/L, respectively. Granular ferric hydroxide (GEH 104) was provided by GEH Wasserchemie GmbH. The adsorbent particles were sieved to a size range of 0.5–1.25 mm for all experiments. The initial structural and compositional characteristics of fresh GEH are presented in Fig. S1.

2.2. Adsorption and regeneration experiments

All experiments were conducted in batch mode in a shaking incubator at 20 ± 1°C and consisted of repeated adsorption, regeneration, and neutralization cycles.

Adsorption: Each test was conducted with 0.2 *g* of GEH in 100 mL of P solution (15 mg/L), with or without Ca (60 mg/L) and NOM (60 mg/L). During adsorption, the solution pH was maintained at 7.5 ± 0.2 by periodic adjustment with 1 M NaOH and HCl. The solution pH and Ca concentration were selected to reflect typical conditions of secondary wastewater effluent, based on the measured data from the Leeuwarden wastewater treatment plant (WWTP) (Table S1). P and NOM concentrations and the 4 d adsorption period were intentionally increased relative to typical effluent conditions to accelerate loading and reveal cycle-dependent deterioration. Control experiments confirmed no visible bulk Ca-P precipitation, and time-resolved samples were collected to evaluate within-cycle uptake before the endpoint. The samples were shaken at 140 rpm for 4 d Water samples were collected during adsorption to obtain time-resolved P removal profiles and to evaluate within-cycle adsorption behavior before the endpoint. Four experimental groups were prepared and named based on the elemental composition of the solution: (1) P group; (2) P+NOM group; (3) P+Ca group; and (4) P+Ca+NOM group.

Regeneration: After completely removing the remaining solution from the adsorption step, the GEH was rinsed three times with demineralized water. Subsequently, GEH was regenerated by shaking with 10 mL of 1 M NaOH at 90 rpm for 1 h.

Neutralization: GEH was shaken at 140 rpm with 50 mL demineralized water, with or without 0.001 M HCl. Three conditions were applied: (1) Rapid rinsing (RR): Shaking with demineralized water for 30 min; (2) Thorough washing (TW): Repeated washing with demineralized water (renewed every 30 min) until the water pH stabilized at around 10; and (3) Acid-assisted neutralization (AN): after the wash water pH had reached around 10, 0.001 M HCl acid wash was added and shaken for 16 h, then rinsed three times with demineralized water. Acid-solution pH was monitored for 16 h to estimate apparent H^+ consumption as an operational indicator of neutralization time. These conditions imposed different residual alkalinity levels rather than optimized protocols.

During the first 12 adsorption-regeneration cycles, all experimental groups were operated under the three neutralization conditions to investigate the impact of neutralization approach and extent on the

long-term performance of GEH under varying water matrices. Due to significant GEH performance deterioration in the P+Ca and P+Ca+NOM groups under the RR and TW conditions, the full AN procedure was applied to these two groups from the neutralization step of cycle 12 onward. Four additional AN treatments were conducted by the end of cycle 15 to evaluate the potential for partial performance recovery.

2.3. Analytical methods

Elemental concentrations (e.g., P, Ca, and iron (Fe)) were measured by inductively coupled plasma-optical emission spectrometry (ICP-OES, iCAP™ PRO, Thermo Fisher Scientific Inc., USA). DOC and inorganic carbon (IC, carbonate, CO_3^{2-}) were measured by total organic carbon analyzer (TOC-L CPH, Shimadzu Ltd., Japan). Organic matter in the regenerant was quantified and characterized by liquid chromatography-organic carbon detection (LC—OCD) analysis (Model 8, DOC-Labor GmbH, Germany), providing DOC concentration and fractionation into biopolymers, humic substances, building blocks, and low-molecular-weight (LMW) organics. pH was measured using a pH meter (InLab® Expert Pro-ISM, Mettler Toledo Inc., USA). All liquid samples were filtered through 0.45 μm filters before analysis, and regenerants were neutralized with 1 M HCl before filtration.

Adsorbent characterization was conducted after drying the samples at 50 °C for 20 h. Specific surface area (SSA) was determined via nitrogen adsorption-desorption isotherms using Micromeritics TriStar 3000, with pore characteristics calculated based on the Brunauer-Emmett-Teller (BET) theory and Barrett-Joyner-Halenda (BJH) model. Surface functional groups were analyzed by attenuated total reflectance-Fourier transform infrared spectroscopy (ATR-FTIR, ALPHA II, BRUKER Inc., Germany). ATR-FTIR band assignments are summarized in Table S2. Adsorbent morphology and elemental composition, including P and Ca, were examined by scanning electron microscopy coupled with energy-dispersive X-ray spectroscopy (SEM-EDX, JEOL-6480LV, JEOL Ltd., Japan). To visualize P and Ca penetration within the adsorbent, cross-sectional SEM-EDX analysis was performed on GEH particles embedded in tissue freezing medium (Leica Inc., USA) and cryo-sectioned using a cryostat microtome (CM1850, Leica Inc., USA). The penetration depth was estimated from SEM-EDX maps using ImageJ (NIH, USA). Two particles with four surface-to-interior transects were analyzed per sample. The external GEH surface was identified from the Fe EDX map as the boundary of the Fe-rich adsorbent region. The Ca and P penetration depths were then estimated as the distances from this boundary over which the corresponding EDX signals remained enriched above the background level toward the particle interior. The Fe speciation of GEH before and after use was determined using Mössbauer spectroscopy (MS). Transmission ^{57}Fe MS spectra were measured at 4.2 K (liquid helium). The MS spectra were collected with conventional constant-acceleration or sinusoidal-velocity spectrometers using a ^{57}Co (Rh) source. The MS spectra, calibrated to α-Fe, were analyzed with MossWinn 4.0 software (Klencsár, 1997).

2.4. Assessment of residual alkalinity

Adsorption and precipitation reactions primarily occurs within GEH micropores and may be affected by local chemical conditions (Suresh Kumar et al., 2019a, 2017), which can differ from the bulk solution pH (Lei et al., 2018; Y. Zhang et al., 2019). However, direct measurement of true intra-particle pH is technically challenging. Therefore, in this study, a grinding-based pH test was used as a comparative indicator of residual alkalinity after different neutralization conditions.

Briefly, 0.2 g of wet GEH sample was mixed with 10 mL of demineralized water, and the suspension pH was recorded before grinding. The GEH granules were then thoroughly ground to expose the internal particle matrix and release pore-associated and surface-associated acid/base species, after which the suspension pH was measured again. The test was performed in triplicate for each condition, including fresh GEH as a control to distinguish the grinding-induced response from residual alkalinity after regeneration.

The apparent OH^- concentration shift was calculated from the paired pH values before and after grinding as $10^{pH_{after}-14} - 10^{pH_{before}-14}$. This value was used only as a comparative indicator of residual alkalinity retained within GEH.

2.5. Data treatment

Data analysis was conducted using Excel and Origin 2018. The amounts of target components removed after adsorption, released during adsorption and regeneration, and retained after regeneration are reported as loadings (mg/g GEH). Removal, regeneration efficiency, retained loading, and Ca/P molar ratios were derived from mass balance calculations for each cycle. Details are provided in the Supporting Information. Unless otherwise stated, symbols in line plots represent individual duplicate measurements, while connecting lines represent the corresponding mean values. For bar plots, bars represent mean values and error bars indicate standard deviations of duplicate measurements. Differences between the experimental groups were evaluated using a paired t-test, with adsorption-regeneration cycle treated as the pairing factor. For each cycle, duplicate measurements were averaged prior to statistical analysis. Statistical significance was assessed at $p < 0.05$.

3. Results

3.1. Rapid rinsing (RR): Ca deteriorates long-term adsorption and regeneration performance

After strong alkaline regeneration, RR did not fully remove residual alkalinity. Grinding increased the suspension pH from 9.8 ± 0.1 to 11.0 ± 0.1, corresponding to an apparent OH^- concentration shift of 1.0 ± 0.2 mM (Table S3).

In the absence of Ca, both the P and P+NOM groups stabilized after the 3rd cycle, with P removal of 1.82–1.96 mg/g and regeneration efficiencies of 96%−97% (Fig. 1a). No significant difference was observed between these groups ($p > 0.05$). NOM removal remained stable at ~1.24 mg/g (Fig. S2a). Retained P remained limited (0.56–0.78 mg/g after 12 cycles; Fig. 1b), and ATR-FTIR spectra exhibited only weak and broadened ν_3 (PO_4^{3-}) bands at 1096 cm^{-1}, which were attributed to bidentate PO_4^{3-} species (Fig. 2a, Table S2).

Conversely, the presence of Ca led to rapid deterioration in the P+Ca group. P removal declined from 7.79 to 2.83 mg/g after the 4th cycle, and regeneration efficiency dropped from 84% to 10% (Fig. 1a). After 12 cycles, retained P and Ca reached 26.78 and 62.18 mg/g, respectively (Fig. 1b). The removed Ca/P molar ratio in each cycle increased sharply after the 5th cycle, peaking at 1.46, while the retained Ca/P ratio decreased from 3.67 to 1.80 (Fig. S4a). From the 6th cycle onward, the removed Ca/P molar ratio decreased during each adsorption cycle, reaching 1.50 by the end of adsorption (Fig. S5a). The ATR-FTIR spectra showed a characteristic PO_4^{3-} band at 1096 cm^{-1}, which is common to both surface-complexed PO_4^{3-} and Ca-P phases. The presence of the ν_1 band at 964 cm^{-1} and the split ν_4 bands at 565/606 cm^{-1} is consistent with hydroxyapatite (HAP)-like Ca-P features, but does not confirm pure HAP. Additionally, carbonate-related bands at 871, 1417, and 1454 cm^{-1} suggested carbonate incorporation (Fig. 2a, Table S2). SEM-EDX images showed clear co-localization of Ca and P, with dense surface aggregates and needle-like morphology, and cross-sectional EDX map showed penetration depths of ~26 μm (Fig. 2b-d, Fig. 3a, b). BET and BJH analyses further indicated changes in pore structure after use, including a marked decrease in SSA and increases in average pore diameter and apparent total pore volume, accompanied by a shift in pore size distribution from smaller mesopores (3–8 nm) toward larger mesopores (5–15 nm) (Table 1; Fig. S8). The reduced difference between adsorption and desorption pore volumes, i.e., a smaller separation between N_2

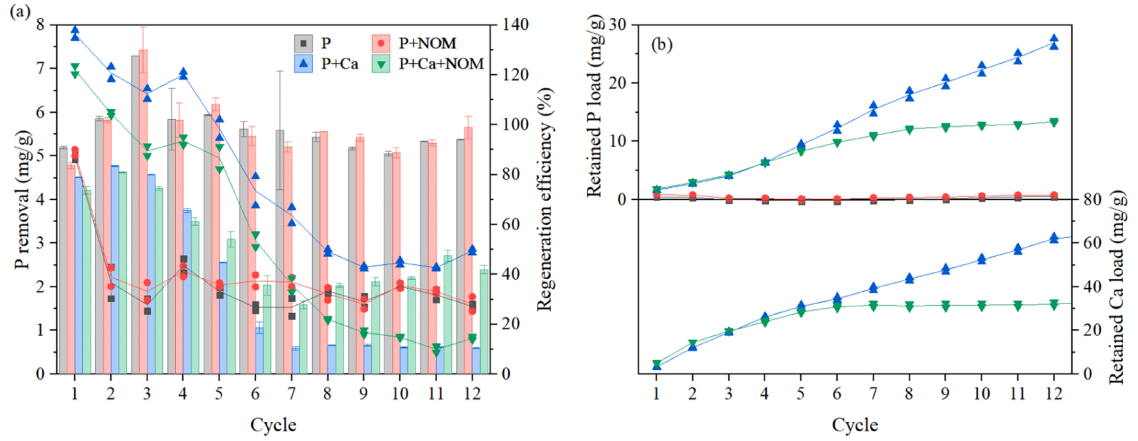

Fig. 1. Adsorption-regeneration performance of GEH under RR. (a) P removal (lines) and regeneration efficiency (bars) and (b) retained P and Ca on GEH over 12 cycles.

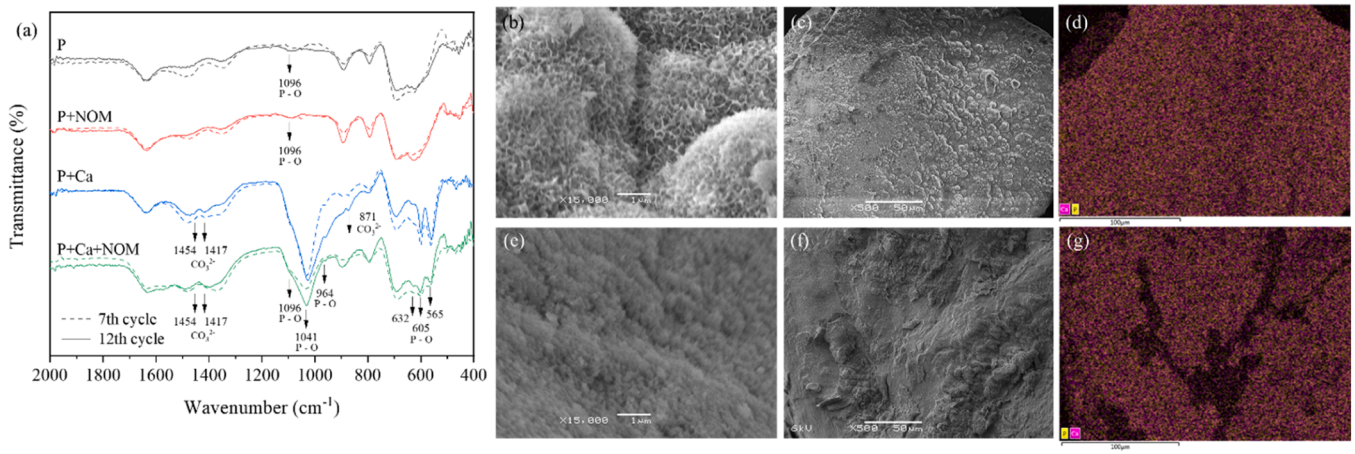

Fig. 2. Characterization of GEH surface under RR. (a) ATR-FTIR spectra after the 7th and 12th adsorption; (b, c) SEM images of GEH surface from the P+Ca group; (e, f) SEM images of GEH surface from the P+Ca+NOM group after the 12th regeneration; (d, g) corresponding EDX elemental maps of (c) and (f). In EDX maps, P is shown in yellow and Ca in magenta.

adsorption and desorption paths, further indicated decreased hysteresis after use.

In the P+Ca+NOM group, regeneration efficiency remained higher than that in the P+Ca group (42%), but adsorption performance declined further to 0.82 mg/g (Fig. 1a). From the 5th cycle onward, Ca removal during adsorption decreased sharply to 0.57 mg/g, accompanied by the release of 0.50 mg/g during regeneration (Fig. S3a). Accordingly, the removed Ca/P molar ratio decreased continuously within each adsorption cycle and approached < 1 at the end of adsorption (Fig. S4a and Fig. S5a). NOM removal peaked at 10.01 mg/g in the 2nd cycle, then decreased rapidly and stabilized at only 1.06 mg/g (Fig. S2a). Retained P (13.26 mg/g), Ca (31.12 mg/g), and NOM (23.21 mg/g) plateaued after cycle 5, a behavior unique to this group (Fig. 1b). ATR-FTIR spectra (Fig. 2a) showed PO_4^{3-} and CO_3^{2-} bands similar to those in the P+Ca group, but with lower intensity and broader ν_3 features (1000–1100 cm^{-1}). SEM images showed more amorphous and loosely aggregated surface deposits (Fig. 2e). EDX mapping still indicated co-localization of Ca and P, but with increasingly irregular surface voids from cycle 7 to 12 (Fig. 2f, g, Fig. S9).

3.2. *Thorough washing (TW): Limited improvement of long-term performance*

To further reduce residual alkalinity, GEH was subjected to TW with demineralized water. This approach reduced the alkaline response after grinding, with the suspension pH increasing from 8.9 ± 0.1 to 10.0 ± 0.2 and the apparent OH^- concentration shift decreasing to 0.1 ± 0.1 mM (Table S3).

In the absence of Ca, performance under TW was similar to that under RR, with P removal stabilizing at 2.14–2.30 mg/g and regeneration efficiency remaining above 95%.

In the P+Ca group, performance declined gradually from the 5th cycle onward. P removal decreased from 6.81 to 2.55 mg/g, while regeneration efficiency decreased from 88% to 20% after 12 cycles (Fig. 4a). Retained P and Ca were 23.08 and 52.88 mg/g, respectively (Fig. 4b). The retained Ca/P ratio decreased to 1.80 after the 11th cycle, approaching the value observed under RR (Fig. S4b). ATR-FTIR spectra showed broadened PO_4^{3-} bands after the 7th cycle, which became sharper by the 12th cycle, while SEM-EDX indicated deeper Ca-P penetration (~37 μm) compared to RR (Fig. 3c, d; Fig. 5a).

In the P+Ca+NOM group, P removal declined from 6.50 to 2.22 mg/g, and regeneration efficiency decreased from 86% to 45% (Fig. 4a). Retained P, Ca, and NOM reached 16.80, 42.42, and 27.66 mg/g, respectively (Fig. 4b). Ca removal was higher than under RR, with only trace amounts (0.15 mg/g) released during regeneration (Fig. S3b). SEM-EDX showed less pronounced surface voids compared to RR (Fig. 5d, e).

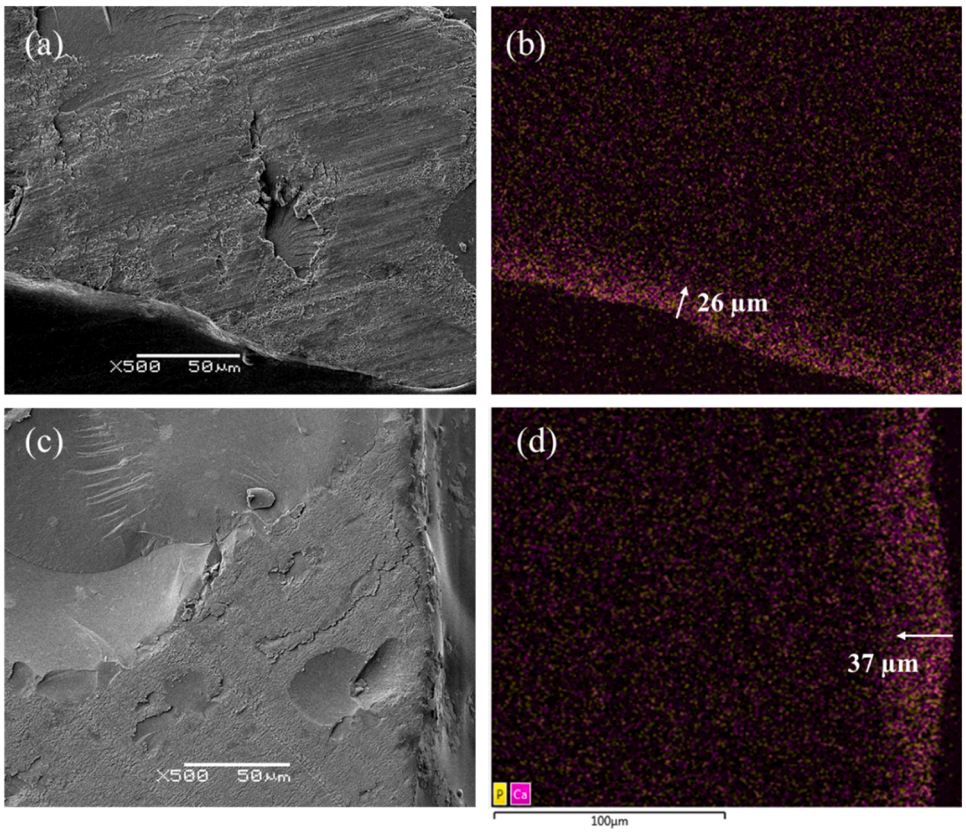

Fig. 3. Characterization of GEH cross-section. (a, c) SEM images of the GEH cross-sections from the P+Ca group after the 12th regeneration under RR and TW; (b, d) corresponding EDX elemental maps of (a) and (c). In EDX maps, P is shown in yellow and Ca in magenta.

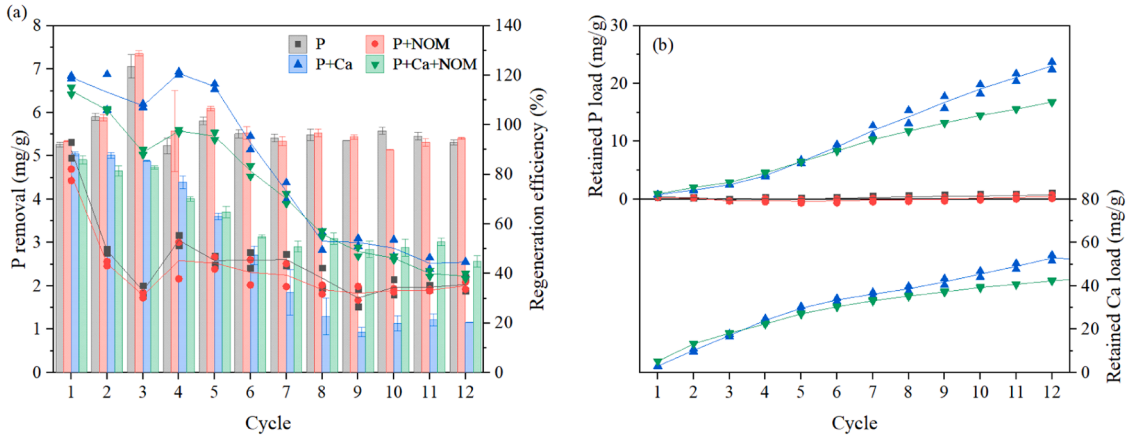

Fig. 4. Adsorption-regeneration performance of GEH under TW. (a) P removal (lines) and regeneration efficiency (bars) and (b) retained P and Ca on GEH over 12 cycles.

3.3. Acid-assisted neutralization (AN): long-term stability

To further reduce residual alkalinity, acid-assisted neutralization was applied after thorough washing, resulting in an apparent OH^- concentration shift of approximately zero after grinding (Table S3).

In the absence of Ca, both the P and P+NOM groups showed improved performance, with P removal of 2.78–2.86 mg/g and regeneration efficiencies of 95%−96%. NOM removal remained limited (~1.30 mg/g, Fig. S2c), consisting mainly of LMW neutrals (0.52 mg/g) and minor humic substances (0.56 mg/g) (Fig. S7c), and showed no significant effect on P removal ($p > 0.05$). ATR-FTIR spectra were similar across conditions, with dominant PO_4^{3-} bands at 1096 cm^{-1}. In the P group, an additional band near 1000 cm^{-1} increased in intensity over cycles, indicating the presence of additional Fe-P surface complexes (Fig. 7a, Table S2).

In the P+Ca group, P removal remained high at 5.83 mg/g, with a regeneration efficiency of 96% over 12 cycles (Fig. 6a). The removed Ca/P molar ratio remained below 1 throughout (Fig. S4c), while retained P and Ca decreased to 4.39 and 23.69 mg/g, respectively. During acid washing, 4.67 mg/g of Ca was released without detectable P (Fig. S11c). The characteristic CO_3^{2-} bands and split ν_4 PO_4^{3-} bands were absent, while the ν_3 PO_4^{3-} band (1000–1100 cm^{-1}) remained with reduced intensity (Fig. 7a). SEM-EDX showed no localized Ca-P enrichment, suggesting limited surface precipitation (Fig. 7c-h).

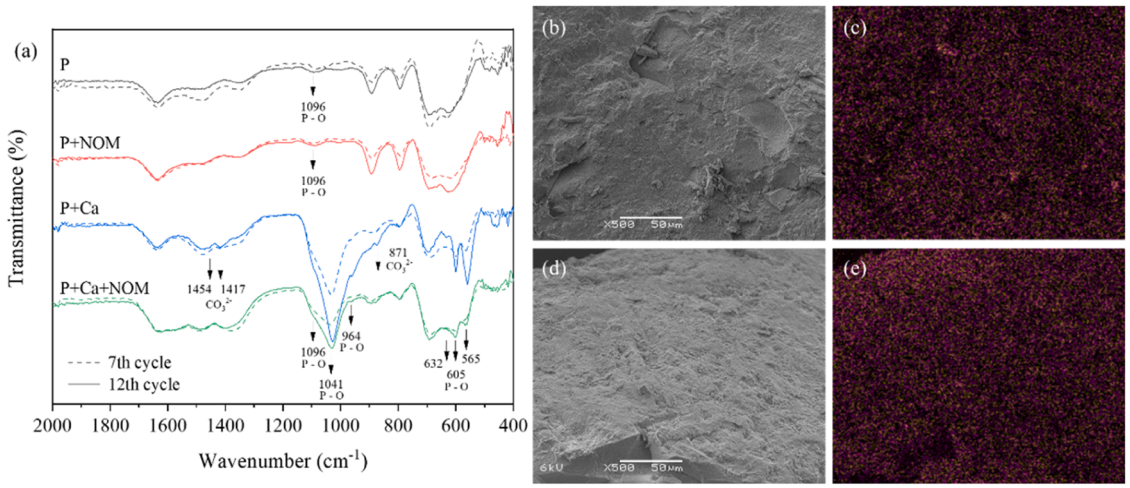

Fig. 5. Characterization of GEH surface under TW. (a) ATR-FTIR spectra after the 7th and 12th adsorption; (b) SEM images and (c) corresponding EDX elemental map of GEH surface from the P+Ca group after the 12th regeneration; (d) SEM images and (e) corresponding EDX elemental map of GEH surface from the P+Ca+NOM group after the 12th regeneration. In EDX maps, P is shown in yellow and Ca in magenta.

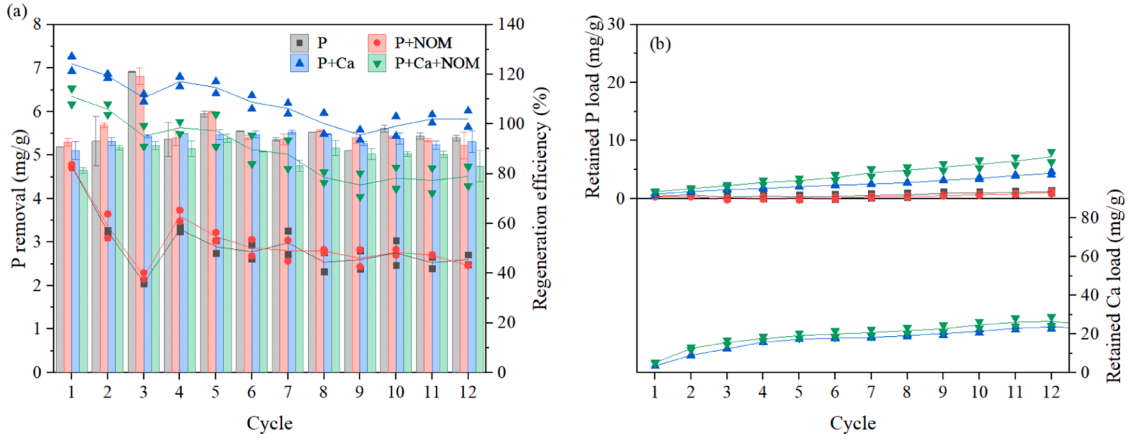

Fig. 6. Adsorption-regeneration performance of GEH under AN. (a) P removal (lines) and regeneration efficiency (bars) and (b) retained P and Ca on GEH over 12 cycles.

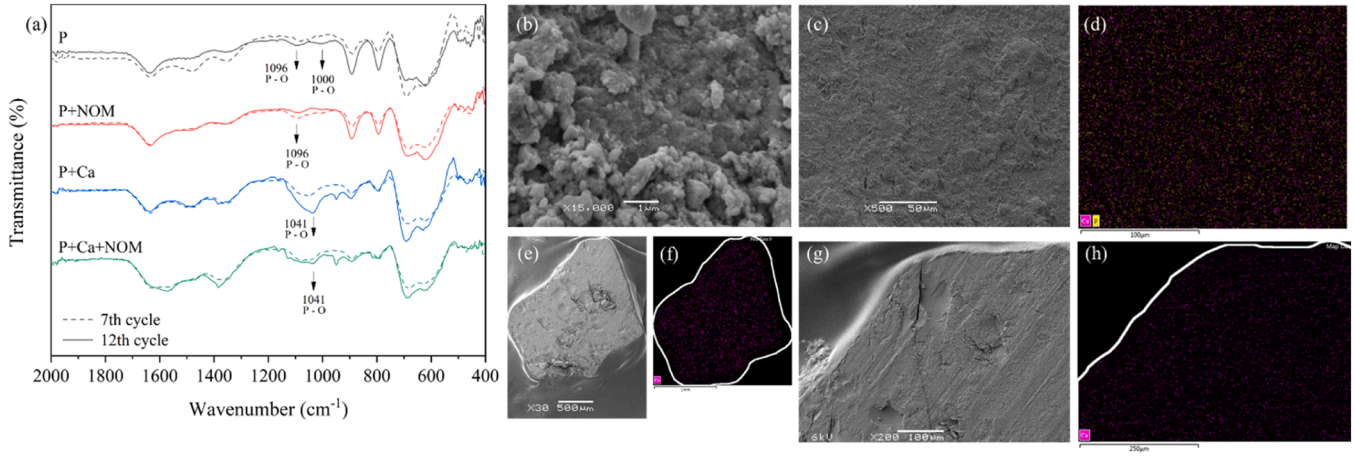

Fig. 7. Characterization of GEH under AN. (a) ATR-FTIR spectra after the 7th and 12th adsorption; (b, c) SEM images of GEH surface and (e, g) SEM images of GEH cross-sections from the P+Ca group after the 12th regeneration; (d, f, h) corresponding EDX elemental maps of (c), (e), and (g). In EDX maps, P is shown in yellow and Ca in magenta.

Similarly, the P+Ca+NOM group maintained high performance, with P removal of 4.51 mg/g and a regeneration efficiency of 88% (Fig. 6a). Time-resolved P removal profiles for representative cycles (Fig. S12) further showed that the performance advantage of AN in Ca-containing systems developed progressively during adsorption as cycling proceeded, rather than only appearing at the 96 h endpoint. Ca and NOM removal stabilized at 5.19 and 5.03 mg/g, respectively (Fig. S2c, S3c). The removed Ca/P molar ratio remained below 1 (Fig. S5c), and Ca release during regeneration remained limited (~0.87 mg/g) compared with RR, while 4.07 mg/g was released during acid washing (Fig. S11c). Retained P (7.22 mg/g) and Ca (27.05 mg/g) were lower than under RR and TW, whereas NOM loading was higher (37.31 mg/g). ATR-FTIR spectra were similar to those of the P+Ca group, with attenuated PO_4^{3-} bands at 1041 cm^{-1} (Fig. 7a). LC—OCD analysis showed enhanced NOM release during regeneration, including 2.83 mg/g humic substances and 0.55 mg/g LMW neutrals (Fig. S7c), without significantly affecting P removal compared with the P+Ca group ($p > 0.05$).

The cumulative Fe release during exposure to 0.001 M HCl over 12 cycles remained very low, ranging from 7.0 ± 0.5 to 17.8 ± 18.0 μg/g (Table S4). This corresponds to less than 0.004% of the Fe content of GEH.

3.4. Delayed acid washing: contrasting recovery

After 12 cycles, the P+Ca and P+Ca+NOM groups under RR and TW conditions were subjected to four additional cycles using the AN protocol to evaluate performance recovery. The final pH of the acid solutions followed the order RR (7.1) > TW (6.9) > continuous AN (6.5), indicating that residual alkalinity from prior operation influenced acid consumption.

In the P+Ca group, acid washing partially recovered performance, but recovery remained incomplete after four cycles, particularly under RR conditions. P removal initially decreased to 1.27–1.79 mg/g at cycle 13, followed by gradual recovery to 2.06–2.95 mg/g. In contrast, regeneration efficiency improved immediately to 33%−48% (RR) and 64%−68% (TW) (Fig. 8a, b). Ca removal decreased to 1.16–1.19 mg/g and remained stable thereafter (Fig. S3). P was detected in the acid solution and increased over successive cycles (0.18 to 0.81–1.20 mg/g), while no P was observed under continuous AN condition. Ca dissolution showed a delayed increase, rising from 0.34–0.40 mg/g in the first acid wash to 5.02–5.17 mg/g after four cycles. Overall, acid washing released 3.36–5.13 mg/g Ca, while retained P remained relatively stable (Fig. S13).

In the P+Ca+NOM group, acid washing improved GEH performance more effectively. P removal increased to 3.56–3.95 mg/g, with regeneration efficiencies reaching 88%−96% (Fig. 8a, b). Simultaneously, Ca and NOM removal increased, while Ca release during regeneration ceased (Figs. S2, S3). P release in the acid solution peaked at cycle 13 (0.72–0.87 mg/g) and then declined, whereas Ca dissolution again exhibited a delayed increase (Fig. S11). Despite performance recovery, retained P and Ca remained higher than under continuous AN condition, at 12.80–16.80 mg/g and 31.02–40.93 mg/g, respectively (Fig. S13).

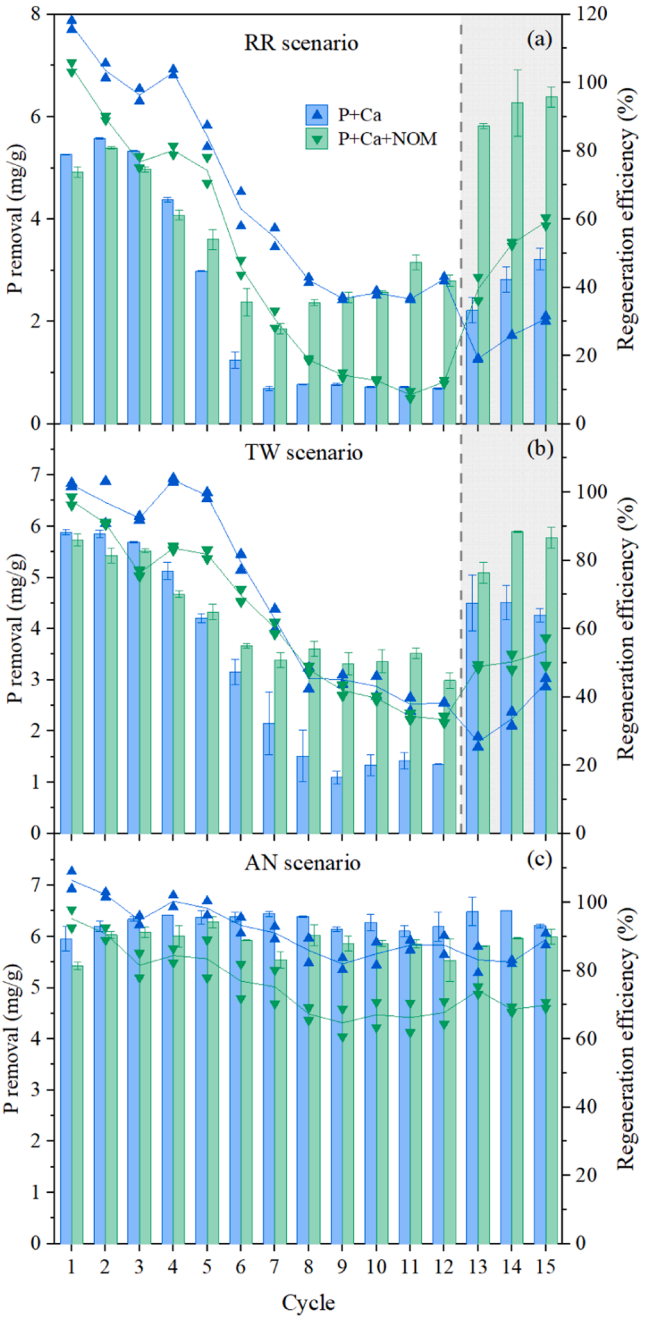

Fig. 8. Adsorption-regeneration performance of GEH of the P+Ca and P+Ca+NOM groups under (a) RR, (b) TW, and (c) AN. P removal is shown as lines, and regeneration efficiencies as bars. In (a) and (b), the shaded region after the 12th cycle indicates the initiation of acid wash treatment.

4. Discussion

4.1. Residual alkalinity drives Ca-P precipitation and pore blockage

Under water-rinsing conditions, GEH deterioration in the P+Ca group was mainly associated with residual alkalinity after NaOH regeneration. When residual OH^- was not fully removed, residual alkalinity retained within GEH could maintain local alkaline conditions within the pores, favoring Ca-based precipitation and less reversible P removal (Lee et al., 2020; Liu et al., 2001). Under alkaline conditions, initially amorphous Ca-P precipitates (Ca/P = 1.5) may form and subsequently evolve toward more ordered HAP-like Ca-P phases (Ca/P = 1.67) (Deng and Dhar, 2023). This interpretation is consistent with the increasing intensity of the split bands at 565/605 cm^{-1} (Fig. 2a, Table S2) and the retained Ca/P molar ratio approaching ~1.8 (Fig. S4a, b). Carbonate-associated bands and the high inorganic carbon concentration in the NaOH regenerant (525.50 ± 157.99 mg/L) further suggest that carbonate-containing Ca phases may have contributed to the deposits. During subsequent adsorption at near-neutral pH, these carbonate-associated phases may have partially dissolved, re-equilibrated, or interacted with phosphate, contributing to the observed ATR-FTIR features and the decrease in the removed Ca/P molar ratio over time (Fig. 2a; Fig. S5a, b). However, these observations do not definitively identify pure HAP, and the exact Ca-P phase composition and co-precipitation pathways remain uncertain (Cui et al., 2023).

Table 1
Pore properties of fresh and used GEH from the P+Ca group under the RR condition after 12 cycles.

Parameter	Unit	Fresh GEH	Used GEH
BET surface area	m^2/g	260.9	224.8
Total pore volume*	cm^3/g	0.266	0.283
BJH adsorption pore volume	cm^3/g	0.255	0.297
BJH desorption pore volume	cm^3/g	0.188	0.295
Adsorption average pore diameter	nm	4.08	5.06

* Single-point apparent total pore volume at a relative pressure (P/P_0) of 0.97.

Ca-based precipitation likely induced selective pore blockage rather than uniform pore filling. Despite a ~65% loss in adsorption capacity, SSA decreased by only 14%, while the apparent total pore volume and average pore diameter slightly increased (Table 1). This apparent mismatch can be explained by pore-size redistribution. BET-derived SSA is highly sensitive to the accessibility of small mesopores, pore entrances, and high-surface-area internal sites; therefore, blockage of these regions can substantially reduce adsorption accessibility. In contrast, the single-point total pore volume measured at $P/P_0 = 0.97$ represents an apparent N_2-accessible pore volume and may include contributions from larger accessible pores, interparticle voids, or precipitate-associated void spaces (Pignatello et al., 2006). Therefore, the increase in apparent pore volume does not indicate improved adsorption accessibility. Thus, the increased apparent pore volume, loss of mesopores < 5 nm, and increased average pore diameter indicate reduced access to smaller pores and a shift toward larger N_2-accessible voids (Fig. S8). The reduced adsorption-desorption hysteresis further supports altered mesopore connectivity or loss of constricted pore regions after use, consistent with selective pore blockage rather than uniform pore collapse (Rigby and Fletcher, 2004). SEM-EDX further supports this interpretation by showing Ca-P accumulation at the GEH surface and near-surface region (Figs. 2, 3, and 5).

The two water-rinsing conditions mainly differed in the extent of residual alkalinity. The stronger alkaline response under rapid rinsing condition likely promoted faster near-surface Ca-based precipitation and pore blockage, whereas thorough washing reduced this response and allowed deeper Ca-P penetration (~37 vs. ~26 μm; Fig. 3) before HAP-like Ca-P signatures became evident (Figs. 2a and 5a). This prolonged accessibility explains the higher regeneration efficiency observed under the thorough washing condition, although water-only washing was still insufficient to prevent long-term deterioration.

4.2. The conditional role of NOM in Ca-P dynamics

NOM alone did not impair P adsorption, as demonstrated by the comparable performance of P and P+NOM groups under all conditions ($p > 0.05$). This finding contrasts with studies attributing adsorbent deterioration to organic matter without considering matrix interactions (Antelo et al., 2007; Lin et al., 2017b).

In Ca-containing systems, however, NOM modified Ca-based precipitation behavior under water-rinsing conditions. Compared with the P+Ca group, the P+Ca+NOM group showed lower removed Ca/P molar ratios (Fig. S4), greater Ca release during adsorption and regeneration (Figs. 1a and S3), and weaker and broader PO_4^{3-} bands (Fig. 2a). SEM images further showed more amorphous and loosely aggregated surface deposits, while Ca and P EDX maps revealed more irregular surface voids (Figs. 2e-g and S9). These observations suggest that NOM affected the morphology and stability of Ca-P precipitates, although molecular-level NOM-Ca-P associations were not directly identified. Possible mechanisms include Ca complexation by NOM, competition for adsorption sites or surface coverage on GEH, and interference with Ca-P nucleation or deposit growth (Li et al., 2022; Lin et al., 2005; Sindelar et al., 2015). In addition, under alkaline conditions, humic components may become increasingly deprotonated, increasing electrostatic repulsion and promoting disaggregation of NOM-associated structures (Avena and Wilkinson, 2002). This may reduce the cohesion of NOM-containing Ca-based precipitates, making them more susceptible to partial detachment.

Under acid-assisted neutralization condition, NOM effects were much weaker. The P+Ca+NOM group showed only slightly lower P adsorption (1.27 mg/g) and regeneration efficiency (6%) than the P+Ca group. This limited interference may reflect reduced residual alkalinity, which suppressed extensive Ca-based precipitation and shifted NOM effects toward weaker surface-related interactions, such as partial surface coverage or Ca-mediated association with GEH (Antelo et al., 2007; Avena and Wilkinson, 2002; Jiang et al., 2018; W. Li et al., 2018). Overall, NOM was not an independent dominant cause of deterioration under the tested conditions, but acted mainly as a secondary modifier of Ca-associated deposition when Ca and residual alkalinity were both present.

4.3. Acid-assisted neutralization prevents deterioration and amplifies Ca positive effects

Under acid-assisted neutralization, GEH not only maintained stable adsorption capacity across all water matrices, but also preserved higher apparent within-cycle P uptake rates in Ca-containing systems, indicating that residual alkalinity affected both accessible capacity and apparent adsorption kinetics (Fig. S12). Mössbauer spectroscopy indicated minor changes in magnetic ordering after repeated cycling, with a more pronounced contribution of magnetically ordered Fe phases under acid-assisted neutralization condition (Fig. S10 and Table S5). However, these changes were not accompanied by substantial Fe dissolution, as Fe release during acid washing remained very low. The spectral changes were therefore more likely related to gradual structural ordering or aging of the Fe oxide phase rather than acid-induced material loss. Moreover, stable adsorption-regeneration performance was maintained despite these spectral changes, suggesting that adsorption performance deterioration was governed primarily by surface physio-chemical processes associated with residual alkalinity and Ca-based precipitation, rather than by bulk structural transformation of GEH.

The improved performance can be attributed to the reduction of residual alkalinity after regeneration. Reduced residual alkalinity may provide a more favorable local environment for P adsorption. Previous studies have shown that PO_4^{3-} binding modes on iron oxides vary with pH, with bidentate inner-sphere complexes dominating at higher pH and both bidentate and monodentate forms occurring at lower pH (Arai and Sparks, 2001; Zhang et al., 2019). Consistently, ATR-FTIR spectra of the P group (Fig. 7a) show features indicative of both bidentate and monodentate bands, suggesting that reduced residual alkalinity promoted multiple binding modes and enhanced P adsorption. Second, by reducing residual alkalinity, acid-assisted neutralization limited the accumulation of Ca-based precipitates, as evidenced by the absence of clear Ca-P and CO_3^{2-} signals in ATR-FTIR and SEM-EDX analyses (Fig. 7). The consistently low removed Ca/P molar ratios (< 1; Fig. S4c) further indicate that Ca-P precipitation was not the dominant P removal pathway, as $Ca/P = 1$ represents the minimum stoichiometric ratio for Ca-P formation. This suggests that P removal was primarily governed by adsorption, consistent with findings from Lin et al. (2017a). In addition, Ca-P phases are unstable under acidic conditions (pH < 4.5) (Bengtsson et al., 2009; Cui et al., 2023) and may dissolve during acid washing, further limiting their accumulation even if minor precipitation did occur.

At the same time, Ca enhanced P adsorption under the acid-assisted neutralization condition without compromising regeneration. P removal in Ca-containing groups was nearly doubled compared with Ca-free groups, while regeneration efficiency remained high (> 88%). This enhancement may result from Ca bridging and Ca-induced increases in GEH PZC, both of which promote attraction of negatively charged PO_4^{3-} species at pH ~7.5 (Antelo et al., 2015; Cui et al., 2023; Lin et al.,

2017a). Because residual alkalinity was reduced, these beneficial Ca effects were not converted into extensive precipitation, allowing high regenerable P removal to be maintained.

Ca also enhanced NOM removal under the acid-assisted neutralization condition. In the absence of Ca, NOM removal was limited and dominated by weakly interacting LMW neutrals. In Ca-containing group, NOM removal increased by 3.13–6.44 mg/g, mainly due to enhanced removal of the humic fraction (Fig. S7c). This may be attributed to Ca-mediated cation bridging, which promotes the retention of negatively charged humic substances (Jiang et al., 2018; W. Li et al., 2018; Sowers et al., 2018). Although enhanced NOM removal may partially reduce surface accessibility, its impact remained secondary and limited under the acid-assisted neutralization condition.

Overall, previous studies have suggested that Ca can facilitate P removal but hinder regeneration by promoting Ca-P precipitation and adsorbent deterioration (Cui et al., 2023; Gao et al., 2023; Y. Zhang et al., 2019). In contrast, this study shows that acid-assisted neutralization can reduce residual alkalinity after regeneration, limiting precipitation-driven deterioration while preserving the beneficial effect of Ca on P adsorption.

4.4. Limited recovery by delayed acid washing

Delayed acid washing after 12 cycles partially recovered GEH performance, but its effectiveness depended strongly on the water matrix and remained limited compared with continuous acid-assisted neutralization. This indicates that, once Ca-based deposits have accumulated, post-hoc acid washing cannot fully reverse deterioration under the acid dose and contact time applied in this study. Therefore, delayed acid washing should be interpreted as a corrective treatment with limited recovery potential, whereas acid-assisted neutralization is more effective when applied preventively after each alkaline regeneration step.

Acid washing after the 12th cycle released relatively high amounts of P but limited Ca, in contrast to the continuous acid-assisted neutralization condition (Fig. S11). This suggests that acid was initially consumed by neutralizing residual alkalinity retained within GEH before effectively dissolving Ca-P deposits. Because active sites remained partly blocked, the released P was not fully re-adsorbed, leading to detectable P in the acid solution.

In the P+Ca group, the first post-wash adsorption cycle showed an immediate decrease in both P and Ca removal, indicating that direct P adsorption and Ca-associated P removal were temporarily hindered (Fig. 8 and Fig. S3). Acid washing lowered residual alkalinity, but accumulated Ca-based precipitates may still have restricted access to adsorption sites and altered the surface charge condition (Al Mahrouqi et al., 2017; Antelo et al., 2015), making Ca uptake less favorable at the operating pH and thereby suppressing Ca-bridging-mediated P adsorption. Nevertheless, regeneration efficiency increased, suggesting that P removal shifted from precipitation-dominated to adsorption-controlled processes.

In the P+Ca+NOM group, GEH performance recovered more rapidly, with an immediate increase in P removal and regeneration efficiencies reaching 87%−96% (Fig. 8). Ca removal also increased markedly (Fig. S3), indicating faster recovery of Ca-associated P removal. This difference may be related to several factors. First, the less compact and more heterogeneous Ca-based deposits formed in the presence of NOM during earlier alkaline cycles may have left a higher fraction of adsorption sites accessible after acid washing. Second, under the lower-pH post-wash condition, humic components may be less deprotonated, which could reduce Ca detachment from NOM-containing Ca-based deposits compared with the previous alkaline cycles (Avena and Wilkinson, 2002). Third, preloaded negatively charged NOM, together with the lower retained Ca loading, may have partly moderated the increase in effective PZC and maintained more favorable conditions for renewed Ca association. However, the molecular-level NOM-Ca-P associations responsible for this behavior were not directly identified.

Despite gradual improvement, GEH performance remained only partially recovered, especially in the P+Ca group. This incomplete recovery suggests that the applied acid dose was insufficient to fully remove accumulated Ca-based precipitates, possibly because these deposits had aged toward less soluble HAP-like phases during repeated adsorption-regeneration cycles. Nevertheless, performance improved before retained Ca and P were completely removed (Fig. S13), indicating that residual alkalinity, rather than precipitate accumulation alone, was the major driver of deterioration. These results further suggest that delayed acid washing can only partially recover deteriorated GEH, whereas continuous acid-assisted neutralization more effectively prevents deterioration.

4.5. Implications and limitations for regeneration design

The results show that long-term performance of iron oxide-based adsorbents is strongly influenced by residual alkalinity and Ca-based precipitation. Acid-assisted neutralization acted as a preventive residual-alkalinity control step that reduces residual alkalinity before the next adsorption cycle. This suppressed Ca-P precipitation, limited pore blockage, and maintained adsorption-dominated P removal. Post-regeneration neutralization should therefore be considered a control step for maintaining adsorbent lifespan, rather than only a delayed treatment for removing aged precipitates.

The practical relevance of this study lies in adsorbent-side loading and deterioration, not full-scale process design. In fixed-bed operation, the water-phase contact time, expressed as empty bed contact time (EBCT) or hydraulic residence time (HRT), is in the order of minutes, whereas the adsorbent remains in service until breakthrough over a much longer loading period. Multiple columns can operate online while one exhausted column is regenerated offline, so regeneration time does not add to mainstream wastewater HRT. Thus, the 96 h batch exposure represents accelerated adsorbent-side loading, not wastewater HRT. This distinction is consistent with the STOWA BiOPhree pilot, where WWTP effluent was treated by iron-granule columns at minute-scale EBCT with service times of about 1–2 weeks until breakthrough under representative conditions (Oosterhuis et al., 2026). Fig. 9 shows this conceptual configuration. The 16 h acid-assisted neutralization period was not intended to represent an operational cleaning time. Additional pH monitoring showed that most measurable H^+ consumption occurred within the first 4–5 h (Fig. S14). Detailed column sequencing, chemical dosing control, and site-specific techno-economic optimization remain outside the scope of this mechanistic study.

NOM should not be the primary control target, as its effect was secondary to residual alkalinity and Ca interactions.

5. Conclusion

This study identifies post-regeneration residual alkalinity as a critical operational factor controlling the long-term performance of iron oxide adsorbents during cyclic P removal and recovery. Under water-rinsing conditions, residual alkalinity persisted after NaOH regeneration, and Ca-containing systems showed progressive performance deterioration associated with Ca-based precipitate accumulation and pore blockage. This demonstrates that near-neutral bulk pH after rinsing does not necessarily indicate sufficient neutralization of the adsorbent.

In contrast, acid-assisted neutralization reduced residual alkalinity and maintained adsorption-dominated P removal. In Ca- and NOM-containing waters, GEH maintained P removal of 4.51–5.83 mg/g with regeneration efficiencies of 88%−96% over repeated cycles. These results show that Ca can enhance reversible P removal when residual alkalinity is controlled, whereas under residual alkaline conditions it promotes Ca-based precipitation and performance loss. NOM alone had a limited effect, while its influence became more apparent when Ca and residual alkalinity were both present.

Overall, post-regeneration neutralization is a preventive control step

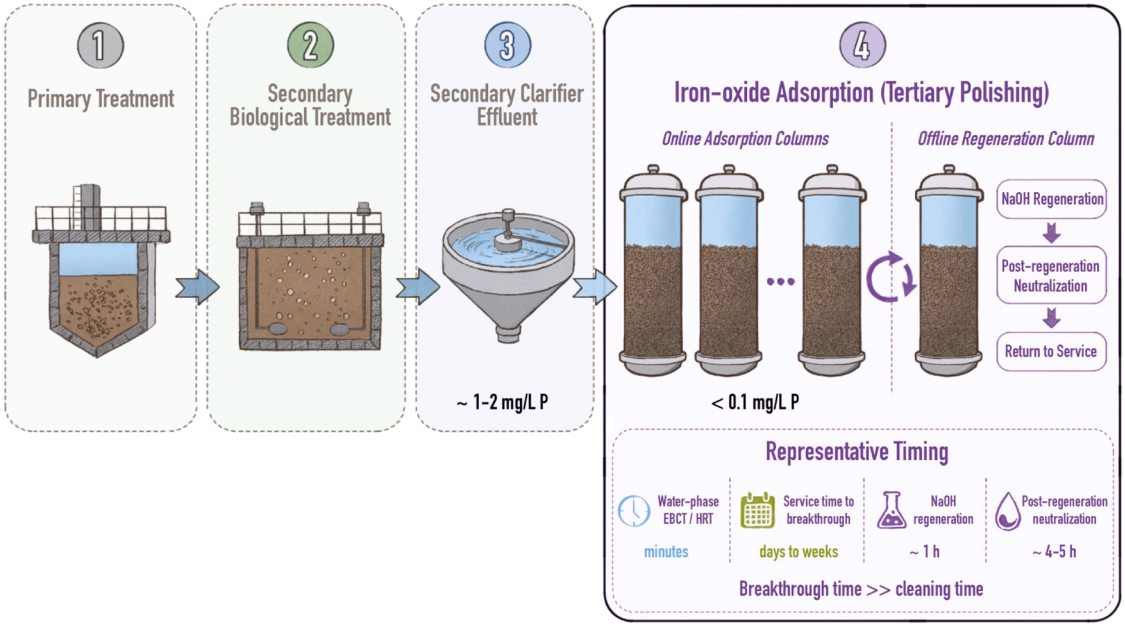

Fig. 9. Conceptual positioning of regenerable iron-oxide adsorption as a tertiary phosphorus-polishing step.

against deterioration rather than a delayed precipitate-removal treatment. These findings guide regeneration protocols for maintaining adsorbent stability during repeated P adsorption–desorption cycles, although continuous-flow validation is still needed to optimize the protocol under realistic conditions.

CRediT authorship contribution statement

Yuwei Huang: Conceptualization, Data curation, Formal analysis, Investigation, Methodology, Visualization, Writing – original draft. **Carlo Belloni:** Conceptualization, Formal analysis, Methodology, Supervision, Validation, Writing – review & editing. **Leon Korving:** Conceptualization, Methodology, Supervision, Writing – review & editing. **A. Iulian Dugulan:** Formal analysis, Investigation, Methodology, Supervision, Validation, Writing – review & editing. **Niels H. van Dijk:** Supervision, Writing – review & editing. **Doris van Halem:** Conceptualization, Methodology, Supervision, Writing – review & editing.

Declaration of competing interest

The authors declare that they have no known competing financial interests or personal relationships that could have appeared to influence the work reported in this paper.

Acknowledgements

This work was performed in the cooperation framework of Wetsus, European Centre of Excellence for Sustainable Water Technology (www.wetsus.nl) co-funded by the Dutch Ministry of Economic Affairs, Ministry of Infrastructure and Environment, European Union Regional Development Fund, Province of Friesland, and Northern Netherlands Provinces. We thank the participants of the research theme "Phosphate Recovery" for their financial support and helpful discussion (Aquacare, Aqua Mineras, GEH Wasserchemie, Haskoning, Kemira, STOWA, VCS Denmark, Waterschap Brabatse Delta, Waterschap Limburg). A special thanks goes to Pim de Jager, Raimonda Buliauskaite, and Laura Herrera Paiva from Aquacare, Simon Kellmann and Carsten Bahr from GEH Wasserchemie, and Mathijs Oosterhuis from Haskoning.

Supplementary materials

Supplementary material associated with this article can be found, in the online version, at doi:10.1016/j.watres.2026.126731.

Data availability

The datasets supporting this study are openly available via 4TU. ResearchData with the DOI:https://doi.org/10.4121/ab29a578-aca4-41e9-aeae-6014b1632114

References

Ai, H., Zhang, K., Penn, C.J., Zhang, H., 2023. Phosphate removal by low-cost industrial byproduct iron shavings: efficacy and longevity. Water Res. 246, 120745. https://doi.org/10.1016/j.watres.2023.120745.

Al Mahrouqi, D., Vinogradov, J., Jackson, M.D., 2017. Zeta potential of artificial and natural calcite in aqueous solution. Adv. Colloid Interface Sci. 240, 60–76. https://doi.org/10.1016/j.cis.2016.12.006.

Antelo, J., Arce, F., Avena, M., Fiol, S., López, R., Macías, F., 2007. Adsorption of a soil humic acid at the surface of goethite and its competitive interaction with phosphate. Geoderma. 138, 12–19. https://doi.org/10.1016/j.geoderma.2006.10.011.

Antelo, J., Arce, F., Fiol, S., 2015. Arsenate and phosphate adsorption on ferrihydrite nanoparticles. Synergetic interaction with calcium ions. Chem. Geol. 410, 53–62. https://doi.org/10.1016/j.chemgeo.2015.06.011.

Arai, Y., Sparks, D.L., 2001. ATR-FTIR spectroscopic investigation on phosphate adsorption mechanisms at the ferrihydrite-water interface. J. Colloid Interface Sci. 241, 317–326. https://doi.org/10.1006/jcis.2001.7773.

Avena, M.J., Wilkinson, K.J., 2002. Disaggregation kinetics of a peat humic acid: mechanism and pH effects. Environ. Sci. Technol. 36, 5100–5105. https://doi.org/10.1021/es025582u.

Belloni, C., Korving, L., Witkamp, G.J., Brück, E., Dugulan, A.I., 2023. Effect of goethite doping using elements with different preferential oxidation states for improved reversible phosphate adsorption. J. Environ. Chem. Eng. 11, 110505. https://doi.org/10.1016/j.jece.2023.110505.

Bengtsson, Å., Shchukarev, A., Persson, P., Sjöberg, S., 2009. A solubility and surface complexation study of a non-stoichiometric hydroxyapatite. Geochim. Cosmochim. Acta. 73, 257–267. https://doi.org/10.1016/j.gca.2008.09.034.

Cui, J., Yang, J., Weber, M., Yan, J., Li, R., Chan, T., Jiang, Y., Xiao, T., Li, X., Li, X., 2023. Phosphate interactions with iron-titanium oxide composites: implications for phosphorus removal/recovery from wastewater. Water Res. 234, 119804. https://doi.org/10.1016/j.watres.2023.119804.

Deng, L., Dhar, B.R., 2023. Phosphorus recovery from wastewater via calcium phosphate precipitation: a critical review of methods, progress, and insights. Chemosphere 330, 138685. https://doi.org/10.1016/j.chemosphere.2023.138685.

Deng, Y., Weng, L., Li, Y., Ma, J., Chen, Y., 2019. Understanding major NOM properties controlling its interactions with phosphorus and arsenic at goethite-water interface. Water Res. 157, 372–380. https://doi.org/10.1016/j.watres.2019.03.077.

Gao, X., Zhang, Y., Zhou, M., Sun, X., She, X., Qian, J., Pan, B., 2023. Evolving role of Ca^{2+} on the long-term phosphate adsorption-regeneration performance of nanoconfined hydrated lanthanum oxides: short-term enhancement and long-term inhibition. ACS EST Engg. 3, 509–519. https://doi.org/10.1021/acsestengg.2c00333.

Jiang, L., Li, Y., Shao, Y., Zhang, Y., Han, R., Li, S., Wei, W., 2018. Enhanced removal of humic acid from aqueous solution by novel stabilized nano-amorphous calcium phosphate: behaviors and mechanisms. Appl. Surf. Sci. 427, 965–975. https://doi.org/10.1016/j.apsusc.2017.08.104.

Klencsár, Z., 1997. Mössbauer spectrum analysis by Evolution Algorithm. NIM-B 129, 527–533. https://doi.org/10.1016/S0168-583X(97)00314-5.

Kunaschk, M., Schmalz, V., Dietrich, N., Dittmar, T., Worch, E., 2015. Novel regeneration method for phosphate loaded granular ferric (hydr)oxide - A contribution to phosphorus recycling. Water Res. 71, 219–226. https://doi.org/10.1016/j.watres.2015.01.001.

Lee, I.-H., Lee, J.-A., Lee, J.-H., Heo, Y.-W., Kim, J.-J., 2020. Effects of pH and reaction temperature on hydroxyapatite powders synthesized by precipitation. J. Korean Ceram. Soc. 57, 56–64. https://doi.org/10.1007/s43207-019-00004-0.

Lei, Y., Song, B., Saakes, M., Van Der Weijden, R.D., Buisman, C.J.N., 2018. Interaction of calcium, phosphorus and natural organic matter in electrochemical recovery of phosphate. Water Res. 142, 10–17. https://doi.org/10.1016/j.watres.2018.05.035.

Li, N., Tian, Y., Zhao, J., Zhan, W., Du, J., Kong, L., Zhang, J., Zuo, W., 2018a. Ultrafast selective capture of phosphorus from sewage by 3D Fe_3O_4@ZnO via weak magnetic field enhanced adsorption. Chem. Eng. J. 341, 289–297. https://doi.org/10.1016/j.cej.2018.02.029.

Li, W., Liao, P., Oldham, T., Jiang, Y., Pan, C., Yuan, S., Fortner, J.D., 2018b. Real-time evaluation of natural organic matter deposition processes onto model environmental surfaces. Water Res. 129, 231–239. https://doi.org/10.1016/j.watres.2017.11.024.

Li, X., Xu, Y., Shen, S., Guo, T., Dai, H., Lu, X., 2022. Effects of dissolved organic matter on phosphorus recovery via hydroxyapatite crystallization: new insights based on induction time. Sci. Total Environ. 822, 153618. https://doi.org/10.1016/j.scitotenv.2022.153618.

Lin, J., Zhan, Y., Wang, H., Chu, M., Wang, C., He, Y., Wang, X., 2017a. Effect of calcium ion on phosphate adsorption onto hydrous zirconium oxide. Chem. Eng. J. 309, 118–129. https://doi.org/10.1016/j.cej.2016.10.001.

Lin, J., Zhang, Z., Zhan, Y., 2017b. Effect of humic acid preloading on phosphate adsorption onto zirconium-modified zeolite. Environ. Sci. Pollut. Res. 24, 12195–12211. https://doi.org/10.1007/s11356-017-8873-0.

Lin, Y., Singer, P.C., Aiken, G.R., 2005. Inhibition of calcite precipitation by natural organic material: kinetics, mechanism, and thermodynamics. Environ. Sci. Technol. 39, 6420–6428. https://doi.org/10.1021/es050470z.

Liu, C., Huang, Y., Shen, W., Cui, J., 2001. Kinetics of hydroxyapatite precipitation at pH 10 to 1. Biomaterials 22, 301–306. https://doi.org/10.1016/S0142-9612(00)00166-6.

Oosterhuis, M., Verloo, H., de Jager, P., 2026. Pilot study on advanced phosphorus removal from WWTP effluent using BiOPhree® technology (Research report). In: STOWA Foundation for Applied Water Research. Amersfoort, The Netherlands. ISBN 978.94.6479.133.4Available at https://www.stowa.nl/publicaties/pilot-study-advanced-phosphorus-removal-wwtp-effluent-using-biophreer-technology.

Pignatello, J.J., Kwon, S., Lu, Y., 2006. Effect of natural organic substances on the surface and adsorptive properties of environmental black carbon (char): attenuation of surface activity by humic and fulvic acids. Environ. Sci. Technol. 40, 7757–7763. https://doi.org/10.1021/es061307m.

Rigby, S.P., Fletcher, R.S., 2004. Experimental evidence for pore blocking as the mechanism for nitrogen sorption hysteresis in a mesoporous material. J. Phys. Chem. B 108, 4690–4695. https://doi.org/10.1021/jp031253s.

Schindler, D.W., 1977. Evolution of phosphorus limitation in lakes: natural mechanisms compensate for deficiencies of nitrogen and carbon in eutrophied lakes. Science 195, 260–262. https://doi.org/10.1126/science.195.4275.260.

Sindelar, H.R., Brown, M.T., Boyer, T.H., 2015. Effects of natural organic matter on calcium and phosphorus co-precipitation. Chemosphere 138, 218–224. https://doi.org/10.1016/j.chemosphere.2015.05.008.

Song, Y., Hahn, H.H., Hoffmann, E., Weidler, P.G., 2006. Effect of humic substances on the precipitation of calcium phosphate. J. Environ. Sci. 18, 852–857. https://doi.org/10.1016/S1001-0742(06)60004-1.

Sowers, T.D., Adhikari, D., Wang, J., Yang, Y., Sparks, D.L., 2018. Spatial associations and chemical composition of organic carbon sequestered in Fe, Ca, and organic carbon ternary systems. Environ. Sci. Technol. 52, 6936–6944. https://doi.org/10.1021/acs.est.8b01158.

Suresh Kumar, P., Ejerssa, W.W., Wegener, C.C., Korving, L., Dugulan, A.I., Temmink, H., Van Loosdrecht, M.C.M., Witkamp, G.-J., 2018. Understanding and improving the reusability of phosphate adsorbents for wastewater effluent polishing. Water Res. 145, 365–374. https://doi.org/10.1016/j.watres.2018.08.040.

Suresh Kumar, P., Keesman, K.J., Van Loosdrecht, M.C.M., Witkamp, G.-J., 2019a. Effect of pore size distribution and particle size of porous metal oxides on phosphate adsorption capacity and kinetics. Chem. Eng. J. 358, 160–169. https://doi.org/10.1016/j.cej.2018.09.202.

Suresh Kumar, P., Korving, L., Van Loosdrecht, M.C.M., Witkamp, G.-J., 2019b. Adsorption as a technology to achieve ultra-low concentrations of phosphate: research gaps and economic analysis. Water Res. X 4, 100029. https://doi.org/10.1016/j.wroa.2019.100029.

Suresh Kumar, P., Prot, T., Korving, L., Keesman, K.J., Dugulan, I., Van Loosdrecht, M.C.M., Witkamp, G.-J., 2017. Effect of pore size distribution on iron oxide coated granular activated carbons for phosphate adsorption – Importance of mesopores. Chem. Eng. J. 326, 231–239. https://doi.org/10.1016/j.cej.2017.05.147.

Wang, S.-X., Huang, Y.-X., Wu, Q.-F., Yao, W., Lu, Y.-Y., Huang, B.-C., Jin, R.-C., 2024. A review of the application of iron oxides for phosphorus removal and recovery from wastewater. Crit. Rev. Env. Sci. Tec. 54, 405–423. https://doi.org/10.1080/10643389.2023.2242227.

Zhang, H., Elskens, M., Chen, G., Chou, L., 2019a. Phosphate adsorption on hydrous ferric oxide (HFO) at different salinities and pHs. Chemosphere 225, 352–359. https://doi.org/10.1016/j.chemosphere.2019.03.068.

Zhang, Y., She, X., Gao, X., Shan, C., Pan, B., 2019b. Unexpected favorable role of Ca^{2+} in phosphate removal by using nanosized ferric oxides confined in porous polystyrene beads. Environ. Sci. Technol. 53, 365–372. https://doi.org/10.1021/acs.est.8b05177.